

Gas–Vapor Interplay in Plasmonic Bubble Shrinkage

Mikhail E. Zaytsev, Yuliang Wang, Yuhang Zhang, Guillaume Lajoine, Xuehua Zhang, Andrea Prosperetti, Harold J. W. Zandvliet,* and Detlef Lohse*

Cite This: *J. Phys. Chem. C* 2020, 124, 5861–5869

Read Online

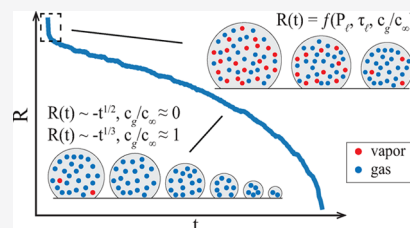
ACCESS |

Metrics & More

Article Recommendations

Supporting Information

ABSTRACT: The understanding of the shrinkage dynamics of plasmonic bubbles formed around metallic nanoparticles immersed in liquid and irradiated by a resonant light source is crucial for the usage of these bubbles in numerous applications. In this paper, we experimentally show and theoretically explain that a plasmonic bubble during its shrinkage undergoes two different phases: first, a rapid partial bubble shrinkage governed by vapor condensation and, second, a slow diffusion-controlled bubble dissolution. The history of the bubble formation plays an important role in the shrinkage dynamics during the first phase as it determines the gas–vapor ratio in the bubble composition. Higher laser powers lead to more vaporous bubbles, while longer pulses and higher dissolved air concentrations lead to more gaseous bubbles. The dynamics of the second phase barely depends on the history of bubble formation, that is, laser power and pulse duration, but strongly on the dissolved air concentration, which defines the concentration gradient at the bubble interface. Finally, for the bubble dissolution in the second phase, with decreasing dissolved air concentration, we observe a gradual transition from a $R(t) \propto (t_0 - t)^{1/3}$ scaling law to a $R(t) \propto (t_0 - t)^{1/2}$ scaling law where t_0 is the lifetime of the bubble and theoretically explain this transition.



INTRODUCTION

Plasmonic nanoparticles immersed in a liquid and irradiated by a resonant laser can rapidly heat up to high temperatures due to their peculiar absorption ability and transfer the heat to the surrounding liquid, causing its heating and subsequent evaporation. The dynamics of these plasmonic bubbles has been extensively studied at the nanoscale^{1–9} as well as at the microscale^{10–16} due to numerous important implications in biomedical therapy,^{17–22} nano/micromanipulation,^{23–27} and enhancement of chemical reactions.^{28,29}

It is important to distinguish between plasmonic nano- and microbubbles. The former are induced around individual nanoparticles by ultrashort highly focused laser pulses. These plasmonic nanobubbles have relatively short lifetimes and sizes in the nanoscale domain.^{2–4,6,7} Plasmonic microbubbles are formed by irradiating an ensemble, for example, a two-dimensional array, of nanoparticles with a laser. The plasmonic microbubbles not only are larger but also live substantially longer.^{11,12,14,16} Recently, it has been shown that plasmonic microbubbles forming on the water-immersed gold nanoparticle arrays under resonant CW laser irradiation undergo four different phases: first, nucleation (and possibly coalescence), growth, and collapse of a giant vapor bubble; second, an oscillating bubble phase; third, bubble growth, which is mainly governed by water vaporization; and fourth, slow bubble growth due to air diffusion from the bulk liquid.^{30,31} Therefore, the interplay between gas and vapor is crucial for the dynamics of plasmonic microbubbles.

After switching off the laser a plasmonic microbubble formed in water does not collapse immediately but remains present on

the substrate for minutes or even hours.^{12,14} That implies that the plasmonic bubble initially partially consists of air and therefore the bubble is quite stable in the liquid. The process of this slow bubble dissolution is governed by air diffusion from highly saturated areas in the vicinity of the bubble to the less saturated bulk liquid. Right before the process of slow bubble dissolution, rapid partial bubble shrinkage occurs during the first milliseconds after switching off the laser due to the fast vapor condensation. The pure vapor bubble collapse has been thoroughly scrutinized in numerous studies,^{32–39} while the collapse of the bubble, which consists of the gas/vapor mixture is still a topic of current research.^{38,40–42} A typical, experimentally obtained, dependence of the plasmonic bubble radius on time during shrinkage is shown in Figure 1.

In our experiments, the influence of various parameters, such as the dissolved air concentration, which can be expressed in terms of the gas saturation level c_g/c_{sat} where c_g is the air concentration and c_{sat} is the saturation air concentration, laser power P_l , and laser pulse duration τ_p , during bubble growth on the subsequent bubble shrinkage is studied. The dynamics of the first phase (condensation-dominated) strongly depends both on the history of bubble formation, that is, laser power and laser pulse length, and on the dissolved air concentration in the water

Received: November 14, 2019

Revised: February 12, 2020

Published: February 17, 2020

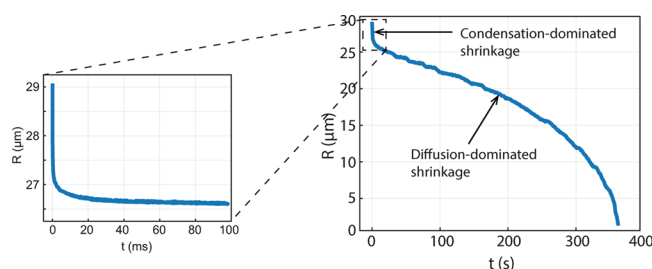


Figure 1. The two different regimes are clearly distinguishable during plasmonic bubble shrinkage: phase 1 - rapid bubble shrinkage governed by vapor condensation and phase 2 - slow bubble dissolution due to air diffusion from the bubble to the bulk liquid.

as they determine the bubble composition right before stopping laser irradiation. The second phase (diffusion-dominated) barely depends on the history of bubble formation but strongly depends on the dissolved air concentration. The dissolved air concentration determines the effective scaling exponent for the bubble radius evolution in time. Our results bear important implications for the design and control of plasmonic microbubbles for various applications.

METHODS

Sample Preparation. A gold layer of approximately 45 nm was deposited on an amorphous fused-silica wafer by using an ion-beam sputtering system (home-built T'COathy machine, MESA+ NanoLab, Twente University). A bottom anti-reflection coating (BARC) layer (~ 186 nm) and photoresist (PR) layer (~ 200 nm) were subsequently coated on the wafer. Periodic nanocolumns with diameters of approximately 110 nm were patterned in the PR layer using displacement Talbot lithography (PhableR 100C, EULITHA).⁴³ These periodic PR nanocolumns were subsequently transferred at the wafer level to the underlying BARC layer, forming 110 nm BARC nanocolumns by using nitrogen plasma etching (home-built TETSKE machine, NanoLab) at 10 mTorr and 25 W for 8 min. Using these BARC nanocolumns as a mask, the Au layer was subsequently etched by ion beam etching (Oxford i300, Oxford Instruments, United Kingdom) with 5 sccm of Ar and 50–55 mA at an inclined angle of 5° . The etching for 9 min resulted in periodic Au nanodots supported on cone-shaped fused-silica features. The remaining BARC was stripped using oxygen plasma for 10 min (TePla 300E, PVA TePla AG, Germany). The fabricated array of Au nanodots was heated to 1100°C in 90 min and subsequently cooled passively to room temperature. During

the annealing process, these Au nanodots re-formed into spherical-shaped Au nanoparticles. Figure 2b shows the schematic of a gold nanoparticle sitting on a SiO_2 island on a fused-silica. The SEM image of the patterned gold nanoparticle sample surface is shown in Figure 2c.

Setup Description. The experimental setup for plasmonic microbubble imaging is shown in Figure 2a. The gold nanoparticle covered sample was placed in a quartz glass cuvette and filled with liquid. A continuous-wave (CW) laser (Cobolt Samba) of a 532 nm wavelength and a maximum power of 300 mW was used for sample irradiation. The size of the laser spot on the sample was $20\ \mu\text{m}$. An acousto-optic modulator (Opto-Electronic, AOTFncVIS) was used as a shutter to control the laser irradiation on the sample surface. Laser pulses were generated and controlled by a pulse/delay generator (BNC model 565). The laser power was controlled by using a half-wave plate and a polarizer and measured by a photodiode power sensor (S130C, Thorlabs). Two high-speed cameras were installed in the setup, one (Photron SA7) equipped with a $5\times$ long-working distance objective (LMPLFLN, Olympus) and the other (Photron SA1) equipped with a $50\times$ long-working distance objective (SLMPLN, Olympus) and operated at various frame rates from 30 fps for the slow (second) phase of bubble shrinkage up to 300 kfps for the first (rapid) phase of bubble shrinkage. The first camera was used for a top view and laser alignment, while the second one was used for a side view. Two light sources, Olympus ILP-1 and Schott ACE I, provided illumination for the two high-speed cameras. The optical images have been processed with an image segmentation algorithm in Python for the extraction of the bubble parameters, such as radius, height, volume, and contact line. During experiments, the nanoparticle-covered sample surface was immersed into deionized water (Milli-Q Advantage A10 System, Germany). Air concentration levels have been measured by an oxygen meter (Fibox 3 Trace, PreSens). For obtaining the air-equilibrated water, a sample bottle containing deionized water was kept open in air for 10 h, and the measured air concentration level is $c_g/c_{\text{sat}} = 0.99$. Partially degassed water with different air saturation levels was prepared by tuning the time of deionized water degassing in a vacuum chamber. Under laser irradiation, gold nanoparticles might melt from the generated heat. The temperature increase of the array of Au nanoparticles can be calculated by a method developed by Baffou et al.⁴⁴ Using this method, we arrive at a temperature increase of approximately 270 K, that is, far below the melting temperature of gold. In

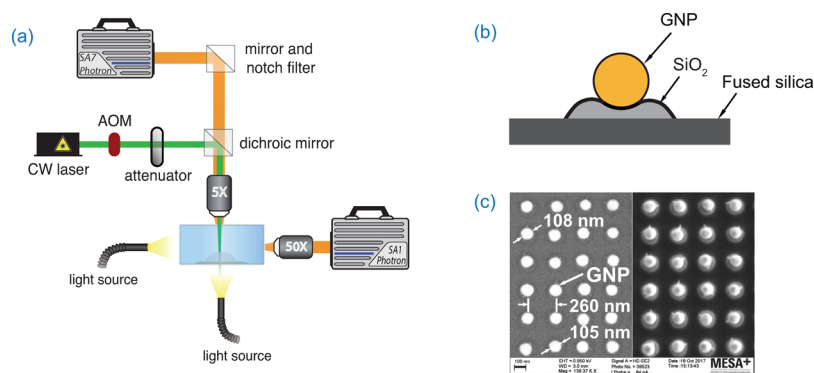


Figure 2. (a) Schematic of the optical imaging facilities for plasmonic microbubble formation observation. (b) Schematic of a gold nanoparticle sitting on a SiO_2 island on a fused-silica substrate. (c) SEM images of the patterned gold nanoparticle sample surface.

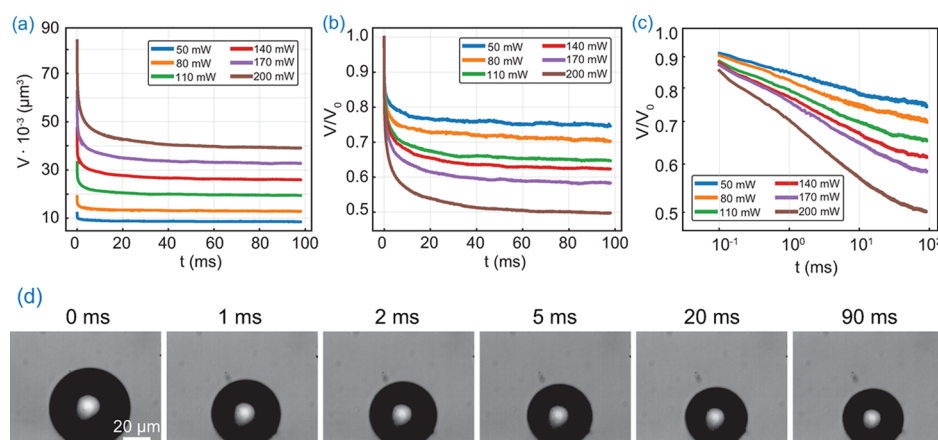


Figure 3. (a) Bubble volume, (b) normalized bubble volume, and (c) normalized bubble volume in the double-logarithmic scale as a function of time right after switching off the laser after 0.1 s of irradiation for various laser powers in water with $c_g/c_{\text{sat}} = 0.99$. (d) Snapshots of plasmonic bubble shrinkage in air-equilibrated water during the first 90 ms after switching off the laser after a 0.1 s laser pulse with a laser power of $P_1 = 200$ mW. The first frame (0 ms) corresponds to the moment when the laser was switched off.

addition, our SEM images recorded after the experiments reveal that the nanoparticles are unaltered (position, size, and shape).

RESULTS AND DISCUSSION

Condensation-Dominated Shrinkage. As was already mentioned, right after turning off the laser, the bubble quickly partially shrinks due to water vapor condensation. To illustrate this process, the bubble volume V and the normalized volume V/V_0 where V_0 is the bubble volume at the moment when we switched the laser off as a function of time during the first 100 ms after 0.1 s of laser irradiation in water with a gas saturation level of $c_g/c_{\text{sat}} = 0.99$ for different laser powers are shown in Figure 3a,b, respectively. One can see that, for all laser powers, rapid bubble shrinkage occurs during the first milliseconds but then slows down followed by a much slower volume reduction. The snapshots of the process in various moments of time are shown in Figure 3d. From Figure 3a, it is clear that, at the specified parameters of $\tau_p = 0.1$ s and $c_g/c_{\text{sat}} = 0.99$, higher laser powers lead to larger bubbles before switching off the laser. At the same time, the initial volume drop is much larger for big bubbles than for the small ones: for the lowest laser power used in the experiments, $P_1 = 50$ mW, the normalized bubble volume drops to 0.75 during the first 100 ms after turning off the laser (Figure 3b), while it reduces to 0.52 for the highest laser power of $P_1 = 200$ mW during the same time period. This finding implies that, in the second case, there is relatively more water vapor in the bubble than in the first case. Indeed, with higher laser powers, more energy can be provided to the system to evaporate the liquid in the vicinity of the bubble.

In a nutshell, for specified parameters (τ_p and c_g/c_{sat}), higher laser powers lead to larger bubbles with larger vapor portions in the total bubble composition, and therefore a greater volume drop during the first milliseconds of bubble shrinkage is observed. It is clear that the bubble behavior during this phase is defined by the bubble composition right before turning off the laser. The previously fixed parameters τ_p and c_g/c_{sat} certainly influence the initial bubble composition as well. In order to thoroughly study these dependences, we have considered a broad range of parameters: laser powers of P_1 : 50, 80, 110, 140, 170, and 200 mW, pulse lengths of τ_p : 0.03, 0.05, 0.1, 0.2, and 0.5 s, and air saturation levels of c_g/c_{sat} : 0.99, 0.79, 0.64, 0.50, and 0.32.

The air–vapor ratio in the total bubble composition can be estimated, assuming that, after the initial rapid partial shrinkage, all the vapor has already condensed and considering the bubble as a pure gas bubble. This assumption is reasonable as the complete vapor bubble condensation occurs in the order of milliseconds.³⁸ Therefore, the slow shrinkage part (almost horizontal part of the lines at Figure 3b) can be linearly fitted and extrapolated to estimate, directly from Figure 3b, the part of the bubble that has been condensed, in other words, what was the vapor portion in the initial bubble composition.

Following the above method, water vapor portions in the total bubble volume as a function of P_1 at various air concentrations for $\tau_1 = 0.5, 0.2, 0.1, 0.05$, and 0.03 s have been estimated and are presented in Figure 4a–e, respectively. First of all, as expected, for all dissolved air concentrations (c_g/c_{sat}) and laser pulse lengths (τ_p), the water vapor fraction $V_{\text{vapor}}/V_{\text{total}}$ increases with increasing laser power. For example, in water with $c_g/c_{\text{sat}} = 0.79$ after 0.5 s of laser irradiation (Figure 4a), the vapor portion in the bubble composition gradually increases from 0.14 to 0.24 with increasing laser power from 50 to 200 mW, respectively. When more power is provided, there is more energy available in the system to evaporate the liquid during bubble growth. One can also notice that, for all pulse lengths and laser powers, bubbles, which have been formed in less saturated water, contain relatively more vapor than the ones generated in water with a higher dissolved air concentration. For example, for $\tau_1 = 0.5$ s, bubbles in water with a 99% air concentration consist of only 0.13–0.21 water vapor, while, approximately, half of the bubble's volume in water with a 32% dissolved air concentration is water vapor. For less saturated water, there is a lack of air to diffuse into the bubble; therefore, the bubbles are more vaporous.

The air volume portion in the initial total bubble volume as a function of P_1 and τ_p for air saturation levels of $c_g/c_{\text{sat}} = 0.99, 0.79, 0.64, 0.50$, and 0.32 is shown in Figure 4f–j, respectively. The air fraction in the bubble rapidly decreases with shortening of the laser pulse, which means that bubbles become more vaporous. A similar trend was observed for all water saturation levels. For example, in water with an air concentration of 99% (Figure 4f), the air portion in the bubble composition under the lowest laser power in our experiments, $P_1 = 50$ mW, decreases from 0.87 to 0.59 with decreasing laser-pulse duration from 0.5 to 0.03 s and decreases from 0.79 to 0.31 for the highest laser power $P_1 = 200$

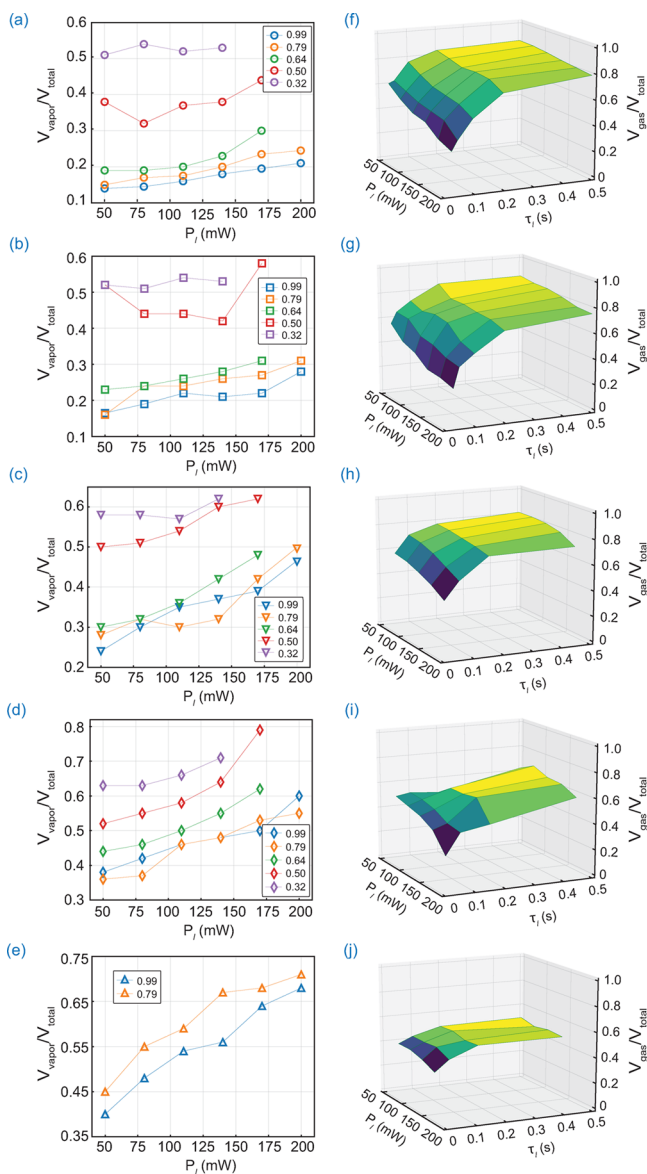


Figure 4. $V_{\text{vapor}}/V_{\text{total}}$ as a function of P_l for $\tau_p =$ (a) 0.5 s, (b) 0.2 s, (c) 0.1 s, (d) 0.05 s, and (e) 0.03 s used for bubble formation and various water saturation levels of $c_g/c_{\text{sat}} = 0.99$ (blue), 0.79 (orange), 0.64 (green), 0.50 (red), and 0.32 (purple); $V_{\text{gas}}/V_{\text{total}}$ as a function of P_l and τ_l for saturation levels of $c_g/c_{\text{sat}} =$ (f) 0.99, (g) 0.79, (h) 0.64, (i) 0.50, and (j) 0.32.

mW. The plasmonic microbubble during its steady growth undergoes two consecutive phases: an initial phase governed by liquid evaporation (~ 10 – 20 ms) and a second phase governed by air diffusion from the bulk liquid (>0.1 s).³⁰ Therefore, for short laser pulses, bubble growth is mainly in the evaporation-controlled regime and there is insufficient time for air to diffuse into the bubble. Therefore, these plasmonic bubbles are more vaporous. With increasing pulse duration, the transition to the diffusive-controlled regime occurs, and therefore these bubbles turn into more gaseous bubbles. It is worth mentioning that, even for the short laser pulses ($\tau_p = 0.03$) during which bubble growth is mainly governed by water evaporation, a considerable amount of air is still present in the bubble, reaching more than half of the bubble volume for low laser powers.

In order to estimate the influence of the initial bubble composition on the first shrinkage phase, one can extract the

effective scaling exponent α from $V(t) \propto t^\alpha$ for the first 5 ms after the end of laser irradiation. The effective scaling exponent as a function of P_l and τ_p is shown in Figure 5a with its projections to

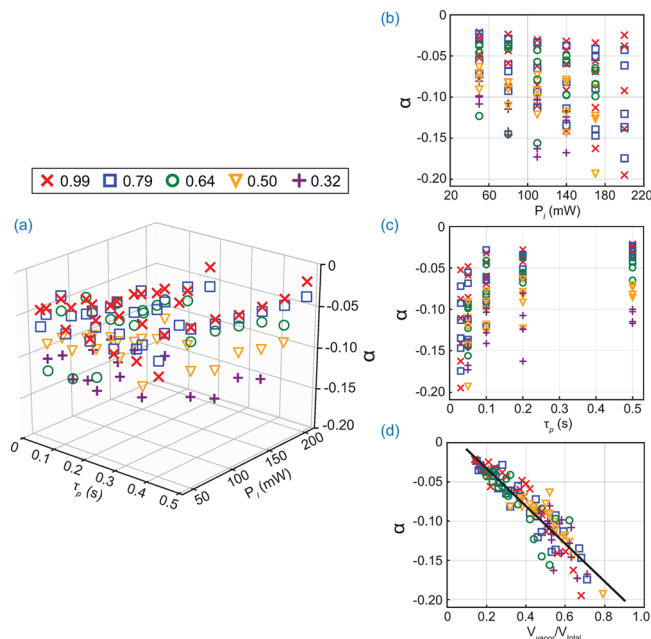


Figure 5. (a) Effective scaling exponent α in the $V(t) \propto t^\alpha$ during the first 5 ms of bubble shrinkage as a function of the pulse length τ_p and laser power P_l , (b) projection to the $\alpha - P_l$ plane, (c) projection to the $\alpha - \tau_p$ plane, (d) effective scaling exponent α as a function of the vapor portion in the initial total bubble composition for various air saturations, c_g/c_{sat} : 0.99 (red cross), 0.79 (blue square), 0.64 (green circle), 0.50 (yellow triangle), and 0.32 (purple cross). For all concentrations, the same dependence of decreasing α values with increasing vapor ratios is observed.

the $\alpha - P_l$ and $\alpha - \tau_p$ planes shown in Figure 5b,c, respectively. No clear dependence can be figured out from these plots. However, it turned out that α strongly depends on the water vapor portion in the initial bubble composition; a clear linear trend can be observed in Figure 5d. The more air is contained in the bubble, the smaller the absolute value of α is. The behavior is universal for all considered P_l , τ_p , and c_g/c_{sat} .

Comparison with the Rayleigh–Plesset Type Model and the Diffusion Equation. For a more quantitative description of the process, we compare our experimental results with a model developed for bubble growth/shrinkage, which takes into account temperature and air diffusion in the liquid and temperature and air–vapor diffusion in the bubble.⁴² The model approximates the bubble as a complete sphere. Both the gas and vapor are assumed to behave like ideal gases. The radial motion of the bubble is described by the Rayleigh–Plesset equation corrected for compressibility effects of the liquid:

$$\left(1 - \frac{\dot{R}}{c_L}\right)R\ddot{R} + \frac{3}{2}\left(1 - \frac{\dot{R}}{3c_L}\right)\dot{R}^2 = \frac{1}{\rho_L}\left(1 + \frac{\dot{R}}{c_L} + \frac{R}{c_L}\frac{d}{dt}\right)\left(p - P - \frac{2\sigma}{R} - 4\mu_L\frac{\dot{R}}{R}\right) \quad (1)$$

where R is the bubble radius, p is the pressure in the bubble, P is the ambient pressure, σ is the interfacial tension coefficient, and ρ_L , μ_L , and c_L is the liquid density, viscosity, and speed of sound;

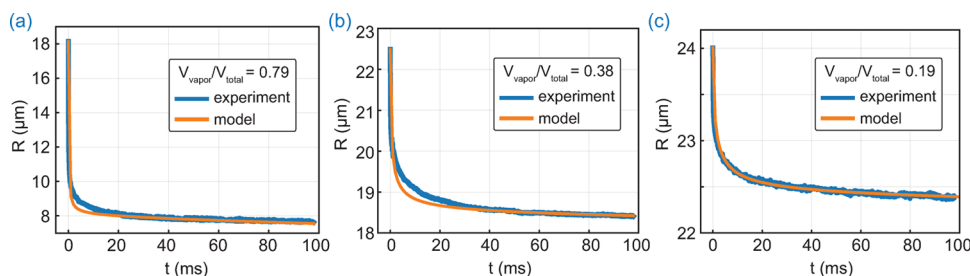


Figure 6. Comparison of the experimental results (blue) and model predictions (orange) of the bubble radius change with time during the first 100 ms after switching off the laser for various initial conditions: (a) $P_1 = 170$ mW, $\tau_p = 0.05$, $c_g/c_{\text{sat}} = 0.5$, and $V_{\text{vapor}}/V_{\text{total}} = 0.79$; (b) $P_1 = 140$ mW, $\tau_p = 0.1$, $c_g/c_{\text{sat}} = 0.99$, and $V_{\text{vapor}}/V_{\text{total}} = 0.38$; and (c) $P_1 = 50$ mW, $\tau_p = 0.5$, $c_g/c_{\text{sat}} = 0.99$, and $V_{\text{vapor}}/V_{\text{total}} = 0.19$.

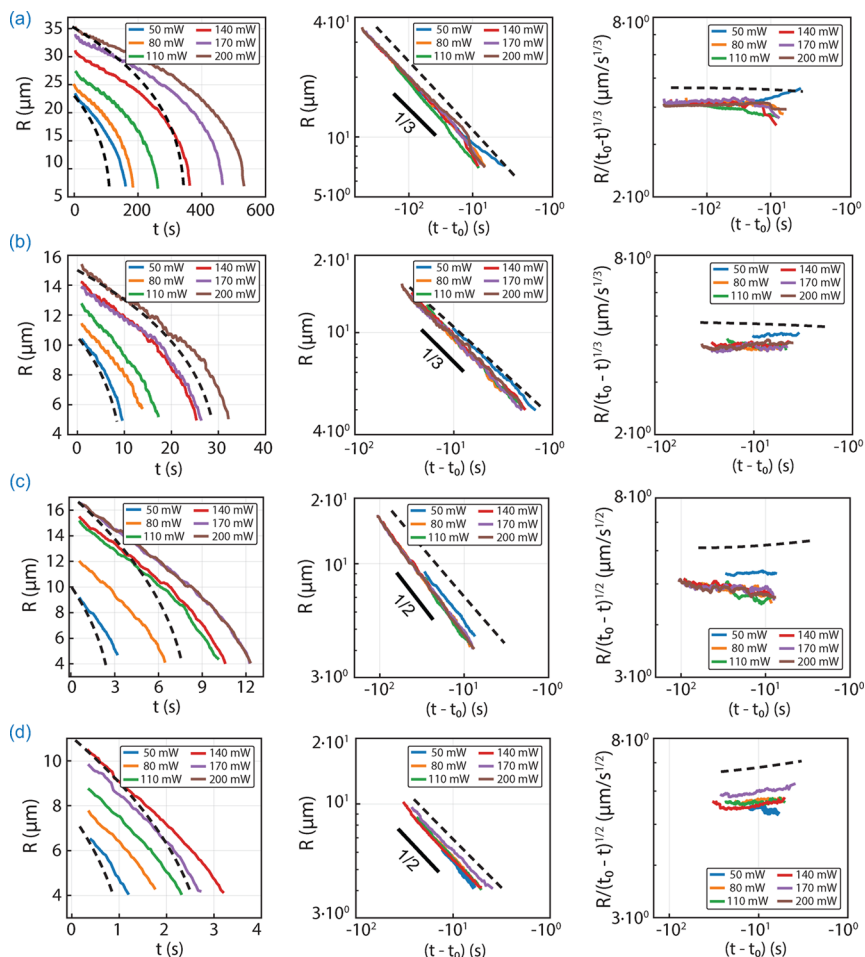


Figure 7. Bubble radius R as a function of time t for various experimental conditions: (a) $c_g/c_{\text{sat}} = 0.99$, $\tau_p = 0.5$ s; (b) $c_g/c_{\text{sat}} = 0.99$, $\tau_p = 0.05$ s; (c) $c_g/c_{\text{sat}} = 0.50$, $\tau_p = 0.5$ s; and (d) $c_g/c_{\text{sat}} = 0.99$, $\tau_p = 0.05$ s, and various laser powers, P_1 : 50 mW (blue), 80 mW (orange), 110 mW (green), 140 mW (red), 170 mW (purple), and 200 mW (brown). The second and third columns represent R as a function of t in the double logarithmic scale and compensated plots $R/(t_0 - t)^{1/3}$ (a, b) and $R/(t_0 - t)^{1/2}$ (c, d) as functions of time in the double logarithmic scale, respectively. Black dashed lines are theoretical curves obtained from the direct solution of the purely diffusive bubble dissolution problem; see text.

the dots denote the time differentiation, and the subscript L is for liquid quantities.

The temperature field in the air–vapor mixture is obtained from the enthalpy equation including the effect of air–vapor diffusion:

$$\frac{\gamma_V}{\gamma_V - 1} \left(1 - \frac{\gamma_G - \gamma_V}{\gamma_V(\gamma_G - 1)} \frac{p_G}{p} \right) p \frac{dT}{dt} = \dot{p} + \nabla \cdot (k \nabla T) + (c_{p,V} - c_{p,G}) \rho D (\nabla C \cdot \nabla T) \quad (2)$$

where k is the thermal conductivity of the air–vapor mixture, c_p is the specific heat at constant pressure, and γ is the ratio of specific heats; indices V and G refer to the vapor and gas, respectively. Furthermore, T is the absolute temperature, dT/dt is the convective derivative, and C is the air concentration by mass. Both the air–vapor velocity field and internal bubble pressure (assumed spatially uniform) are determined from a combination of the continuity and energy equations.⁴²

Conservation of the gas, liquid/vapor, and energy across the bubble interface is imposed. The model is solved numerically by

a spectral method that reduces the problem to a system of ordinary differential equations. In particular, the temperature and concentration fields in the liquid are expressed in a Chebyshev polynomial series in the variable $x = R(t)/r$ with r as the distance from the bubble center. For a more detailed description, the reader is referred to a recent publication.⁴²

The calculation starts at the instant in which the laser is turned off. The measured bubble radius is used as the initial radius. The initial temperature distribution in the liquid is approximated by a fourth-order polynomial even in x . The three coefficients of the linear combination are determined from the ambient liquid temperature, vanishing of the heat flux at $x = 0$ (i.e., at $r \rightarrow \infty$), and surface bubble temperature T_s used as fitting parameters. The initial air concentration in the liquid is approximated in the same way. Given a provisional value for T_s with the assumption of a thermodynamic equilibrium, the partial pressure of the vapor is known, and the partial pressure of air follows from the assumption of a mechanical equilibrium. Through Henry's law, this determines the air concentration at the bubble surface. The air–vapor mixture is assumed to be initially homogeneous at the assumed initial temperature. The results are somewhat dependent on this initial distribution, which cannot be accurately determined from the experiment.

In spite of this uncertainty, it can be seen from Figure 6 that the model is able to reproduce the bubble evolution reasonably well after the laser has been switched off for as long the data were recorded. The error is noticeable during the time in which the bubble shrinkage switches from a condensation-dominated to a diffusion-dominated regime, which is when the influence of the unknown initial temperature distribution in the liquid is particularly significant. Indeed, in Figure 6c, for which the laser power is small and the liquid is nearly saturated with air so that the initial amount of vapor in the bubble is small, the agreement is significantly better than in the other cases. We have found a similar level of agreement for all the dissolved air concentrations that we have tested.

To summarize, the bubble dynamics during the first phase depends on the initial bubble composition, which is defined by the conditions of P_1 , τ_p , and c_g/c_{sat} during bubble growth, that is, on the history of bubble formation, which we can quantitatively describe with the model of ref 42.

Diffusion-Dominated Shrinkage. After the rapid bubble shrinkage, a much slower process takes over. During this phase, the bubble dissolves due to air diffusion from the bubble to the bulk liquid. Our experimental results for laser powers of $P_1 = 50$, 80, 110, 140, 170, and 200 mW, pulse durations of $\tau_p = 0.5$ and 0.05 s, and water with air saturation levels of $c_g/c_{\text{sat}} = 0.99$ and 0.50 are summarized in Figure 7. In Figure 7a, the bubble radii R as a function of time t for $c_g/c_{\text{sat}} = 0.99$ and $\tau_p = 0.5$ s along with a double logarithmic plot and a double logarithmic plot of R compensated with $(t_0 - t)^{1/3}$ are shown where t_0 is the lifetime of the bubble. Figure 7b–d represents the same set of figures but for the following different experimental conditions: $c_g/c_{\text{sat}} = 0.99$ and $\tau_p = 0.05$ s, $c_g/c_{\text{sat}} = 0.50$ and $\tau_p = 0.5$ s, and $c_g/c_{\text{sat}} = 0.50$ and $\tau_p = 0.05$ s, respectively.

As already mentioned, higher laser powers and longer laser pulses lead to larger bubbles, and therefore, at the same ambient conditions, it takes longer for them to completely dissolve. For example, in water with a 99% dissolved air concentration, it takes approximately 100 s for the bubble, which was formed after a laser pulse with $\tau_p = 0.5$ s and $P_1 = 50$ mW and initial radius of $R_0 = 23 \mu\text{m}$, to dissolve, while it takes approximately 550 s for the one formed with $P_1 = 200$ mW and $R_0 = 36 \mu\text{m}$. Bubbles of

comparable sizes dissolve much faster in degassed water than in saturated water, for example, the bubble with $R = 15 \mu\text{m}$ completely dissolves in water with $c_g/c_{\text{sat}} = 0.99$ in approximately 33 s (Figure 7b) while in water with $c_g/c_{\text{sat}} = 0.50$ in 10 s (Figure 7c) due to the larger concentration gradients between the bubble and bulk liquid.

The solid black lines in the double logarithmic plots correspond to the effective scaling exponents of $1/3$ (Figure 7a,b) and $1/2$ (Figure 7c,d) in $R(t) \propto (t_0 - t)^\alpha$ and are shown for a clearer indication of the slope. One can see that, not only for all laser powers but also for all pulse durations, bubbles follow similar dynamics. The double logarithmic plots of R compensated by $(t_0 - t)^{1/3}$ (Figure 7a,b) and $(t_0 - t)^{1/2}$ (Figure 7c,d) further confirm the value of the effective scaling exponent. Despite the slight variations, the scaling exponent remains close to $1/3$ for $c_g/c_{\text{sat}} = 0.99$ and close to $1/2$ for $c_g/c_{\text{sat}} = 0.50$ for all experimental parameters with a fixed air concentration.

In order to further investigate how the concentration of air dissolved in liquid influences the long-term bubble dissolution dynamics, we performed a series of experiments with various c_g/c_{sat} values, namely, $c_g/c_{\text{sat}} = 0.99, 0.79, 0.64, 0.50$, and 0.32 and $\tau_p = 0.5, 0.2, 0.1, 0.05$, and 0.03 s. Performing the same analysis as discussed above for all data sets, the effective scaling exponents (α) in $R(t) \propto (t_0 - t)^\alpha$ for various saturation levels have been extracted (see Figures S1–S4 in the Supporting Information). Remarkably, α only slightly varies with P_1 and τ_p ; however, it strongly depends on the concentration of dissolved air in the liquid. For water with $c_g/c_{\text{sat}} = 0.99$, almost irrespective of P_1 and τ_p , the average effective scaling exponent is always around 0.34. For water degassed till 79% of the saturation air concentration, α increases to 0.41. Further liquid degassing leads to larger scaling exponents, namely, for $f_g = 0.64$, it increases to $\alpha = 0.45$, for $c_g/c_{\text{sat}} = 0.50$ to $\alpha = 0.48$, and for $c_g/c_{\text{sat}} = 0.32$ to $\alpha = 0.50$ (Figure 8). Therefore, what defines the scaling exponent?

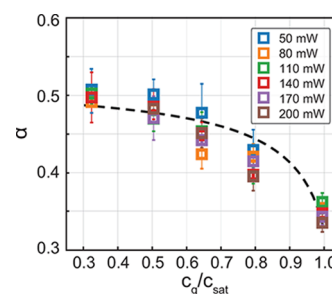


Figure 8. Effective scaling exponent α in $R(t) \propto (t_0 - t)^\alpha$ as a function of air concentration levels for various laser powers, P_1 : 50 mW (blue), 80 mW (orange), 110 mW (green), 140 mW (red), 170 mW (purple), and 200 mW (brown). The dashed black line is the theoretical curve obtained from a complete solution of eq 9 for various air concentrations, showing good agreement with our data.

We consider a spherical purely gas bubble, resting in the surrounding liquid.⁴⁵ Assuming the gas inside the bubble as ideal, that is, $PV = NRT$, and taking into account that the bubble inner pressure is given as a sum of ambient pressure and Laplace pressure, the loss rate of the number, N , of molecules in the bubble can be derived:

$$\dot{N} = \frac{4\pi\dot{R}R^2}{RT} \left(P_\infty + \frac{4\sigma}{3R} \right) \quad (3)$$

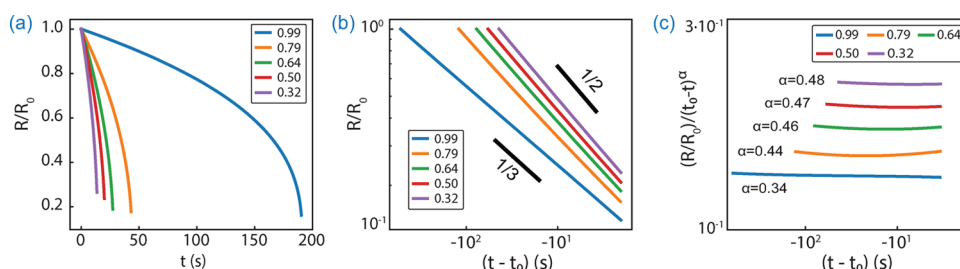


Figure 9. (a) Normalized bubble radius R/R_0 as a function of time t , derived from the solution of eq 9 where $R_0 = 30 \mu\text{m}$. (b) Normalized bubble radius R/R_0 as a function of time t in a double logarithmic scale and (c) compensated plots $(R/R_0)/(t_0 - t)^\alpha$ in the double logarithmic scale where α is an effective scaling exponent for various air saturation levels c_g/c_{sat} : 0.99 (blue), 0.79 (orange), 0.64 (green), 0.50 (red), and 0.32 (purple).

where R is the bubble radius, \mathcal{R} is the ideal gas constant, T is the bubble temperature, P_∞ is the ambient pressure, and σ is the surface tension of the gas–liquid interface.

On the side of the liquid, the molecular flux of air molecules due to diffusion through the bubble interface is determined by the gas concentration gradient

$$\dot{N} = 4\pi R^2 D \left. \frac{\partial c}{\partial r} \right|_{r=R} \quad (4)$$

where D is the mass diffusion coefficient and $c(r, t)$ is the air concentration.

Combining eqs 3 and 4, we have

$$\dot{R} \left(1 + \frac{4}{3} \frac{\sigma}{R P_\infty} \right) \frac{P_\infty}{RT} = D \left. \frac{\partial c}{\partial r} \right|_{r=R} \quad (5)$$

The gas concentration field within the liquid is given by the convection–diffusion equation.

$$\partial_t(c(r, t)) = \frac{D}{r^2} \partial_r(r^2 \partial_r c(r, t)) + \frac{a^2 \dot{a}}{r^2} \partial_r c(r, t) \quad (6)$$

For the majority of the diffusion process, we can make a quasi-steady approximation to the gradient of the dissolved gas concentration at the bubble surface and neglect the time-dependent terms to write

$$\partial_r c|_{r=R} \simeq \frac{c_\infty - c_g|_{r=R}}{R} \quad (7)$$

The dissolved air concentration at the bubble interface, c_g , will be related to the saturated air concentration under a plane interface, c_{sat} , according to Henry's law as

$$c_g|_{r=R} = c_{\text{sat}}(P_\infty) \left(1 + \frac{2\sigma}{R P_\infty} \right) \quad (8)$$

Combining eqs 5, 7, and 8 and introducing $\zeta = 1 - c_\infty/c_{\text{sat}}(P_\infty)$ and $\xi = c_{\text{sat}}(P_\infty)RT/P_\infty$, one can finally obtain

$$\left(1 + \frac{4}{3} \frac{\sigma}{R P_\infty} \right) R \dot{R} = -D \xi \left(\zeta + \frac{2\sigma}{R P_\infty} \right) \quad (9)$$

If one neglects surface tension effects, the equation reduces to

$$R \dot{R} = -D \xi \zeta \quad (10)$$

and can be easily integrated to find $R(t) \propto (t_0 - t)^{1/2}$. Indeed, in our experiments, the effective scaling exponent α was found to be close to 1/2 for degassed water with $c_g/c_{\text{sat}} \leq 0.5$.

The other limiting case is the case of fully saturated liquid, so no concentration gradient exists in the system, that is, $\zeta = 0$.

Omitting the second term in the sum on the left in eq 9, which is generally a small number for bubbles larger than $5 \mu\text{m}$ and setting $\zeta = 0$, we have

$$R \dot{R} = -D \xi \frac{2\sigma}{R P_\infty} \quad (11)$$

from which after integration, one immediately finds the scaling law $R(t) \propto (t_0 - t)^{1/3}$, which is consistent with our experiments for water with $c_g/c_{\text{sat}} = 0.99$.

The complete solution of eq 9 can also be readily found by integration:

$$\begin{aligned} 1 - \frac{R^2}{R_0^2} - 2 \left(1 - \frac{2}{3} \zeta \right) \frac{\Sigma}{\zeta} \left[1 - \frac{R}{R_0} \right. \\ \left. + \frac{\Sigma}{\zeta} \ln \left(\frac{\Sigma/\zeta + R/R_0}{\Sigma/\zeta + 1} \right) \right] \\ = 2 \zeta \xi \frac{D t}{R_0^2} \end{aligned} \quad (12)$$

where $\Sigma = 2\sigma/R_0 P_\infty$.

It is reasonable to assume an effective scaling law for the bubble radius, $R(t) \propto (t_0 - t)^{\alpha(c_g/c_{\text{sat}})}$, where the effective exponent $\alpha = f(c_g/c_{\text{sat}})$ is a function of the dissolved air concentration. The normalized bubble radius R/R_0 where $R_0 = 30 \mu\text{m}$ as a function of time t derived from the analytical solution (eq 12) is shown in Figure 9. One can then extract α from the double logarithmic plot (Figure 9b) using a linear fit. The derived effective exponents are confirmed by the double logarithmic plot compensated by $(t_0 - t)^\alpha$ (Figure 9c) where $\alpha = 0.34, 0.44, 0.46, 0.47$, and 0.48 for $c_g/c_{\text{sat}} = 0.99, 0.79, 0.64, 0.50$, and 0.32 , respectively.

The dependence of α on c_g/c_{sat} resulting from the complete solution (eq 12) for various air saturation levels is shown as a dashed black line in Figure 8. Just as in our experiments with decreasing air concentrations, one can see the gradual transition from the limiting regime where water is almost fully saturated with air and the effective scaling exponent is 1/3 to the regime where we are dealing with large concentration gradients due to water degassing and the 1/2 effective scaling law shows up.

CONCLUSIONS

The dynamics of plasmonic microbubble shrinkage has been studied. During the dissolution, a bubble undergoes two different phases. First, rapid bubble shrinkage due to water vapor condensation occurs in the first milliseconds after switching off the laser. The dynamics of this phase highly depends on the history of bubble formation, which defines the initial bubble composition. The bubble contains more vapor in

its composition and, therefore, shrinks faster for shorter laser pulse durations, lower dissolved air concentrations, and higher laser powers. Afterward, the second phase of slow bubble dissolution takes over, which is governed by air diffusion from the bubble to the bulk liquid and may last up to minutes or even hours. The dynamics of the plasmonic bubble during this phase barely depends on the laser power and laser pulse duration used to form the bubble but strongly depends on the air saturation level in the bulk water as it defines the concentration field in the liquid. The gradual transition from the effective scaling exponent $\alpha = 1/3$ for almost fully saturated water with $c_g/c_{\text{sat}} = 0.99$ to $\alpha \approx 1/2$ for degassed water with $c_g/c_{\text{sat}} \leq 0.5$ has been demonstrated both experimentally and theoretically.

■ ASSOCIATED CONTENT

SI Supporting Information

The Supporting Information is available free of charge at <https://pubs.acs.org/doi/10.1021/acs.jpcc.9b10675>.

Experimental results on the diffusion-dominated phase for water with $c_g/c_{\text{sat}} = 0.99, 0.79, 0.64, 0.50$, and 0.32 for various pulse lengths and laser powers (ZIP)

■ AUTHOR INFORMATION

Corresponding Authors

Harold J. W. Zandvliet – *Physics of Interfaces and Nanomaterials, MESA+ Institute for Nanotechnology, University of Twente, 7500AE Enschede, Netherlands*; orcid.org/0000-0001-6809-139X; Email: h.j.w.zandvliet@utwente.nl

Detlef Lohse – *Physics of Fluids, Max Planck Center Twente for Complex Fluid Dynamics, and J.M. Burgers Centre for Fluid Mechanics, MESA+ Institute for Nanotechnology, University of Twente, 7500AE Enschede, Netherlands; Max Planck Institute for Dynamics and Self-Organization, 37077 Göttingen, Germany*; orcid.org/0000-0003-4138-2255; Email: d.lohse@utwente.nl

Authors

Mikhail E. Zaytsev – *Physics of Fluids, Max Planck Center Twente for Complex Fluid Dynamics, and J.M. Burgers Centre for Fluid Mechanics, MESA+ Institute for Nanotechnology and Physics of Interfaces and Nanomaterials, MESA+ Institute for Nanotechnology, University of Twente, 7500AE Enschede, Netherlands*

Yuliang Wang – *Robotics Institute, School of Mechanical Engineering and Automation, Beihang University, Beijing 100191, P.R. China*; orcid.org/0000-0001-6130-4321

Yuhang Zhang – *Department of Mechanical Engineering, Johns Hopkins University, Baltimore, Maryland 21218, United States*

Guillaume Lajoinie – *Physics of Fluids, Max Planck Center Twente for Complex Fluid Dynamics, and J.M. Burgers Centre for Fluid Mechanics, MESA+ Institute for Nanotechnology and TechMed Centre, University of Twente, 7500AE Enschede, Netherlands*

Xuehua Zhang – *Physics of Fluids, Max Planck Center Twente for Complex Fluid Dynamics, and J.M. Burgers Centre for Fluid Mechanics, MESA+ Institute for Nanotechnology, University of Twente, 7500AE Enschede, Netherlands; Department of Chemical and Materials Engineering, University of Alberta, Edmonton, Alberta T6G 1H9, Canada*; orcid.org/0000-0001-6093-5324

Andrea Prosperetti – *Physics of Fluids, Max Planck Center Twente for Complex Fluid Dynamics, and J.M. Burgers Centre for*

Fluid Mechanics, MESA+ Institute for Nanotechnology, University of Twente, 7500AE Enschede, Netherlands; Department of Mechanical Engineering, Johns Hopkins University, Baltimore, Maryland 21218, United States

Complete contact information is available at:

<https://pubs.acs.org/doi/10.1021/acs.jpcc.9b10675>

Notes

The authors declare no competing financial interest.

■ ACKNOWLEDGMENTS

The authors thank Hai Le The for sample preparation and Xiaojue Zhu for fruitful discussion on numerical simulations. The authors also thank the Dutch Organization for Research (NWO), Netherlands Organisation for Applied Scientific Research (TNO), and Netherlands Center for Multiscale Catalytic Energy Conversion (MCEC) for financial support.

■ REFERENCES

- (1) Kotaidis, V.; Dahmen, C.; von Plessen, G.; Springer, F.; Plech, A. Excitation of Nanoscale Vapor Bubbles at the Surface of Gold Nanoparticles in Water. *J. Chem. Phys.* **2006**, *124*, 184702.
- (2) Lukianova-Hleb, E.; Hu, Y.; Latterini, L.; Tarpani, L.; Lee, S.; Drezek, R. A.; Hafner, J. H.; Lapotko, D. O. Plasmonic Nanobubbles as Transient Vapor Nanobubbles Generated Around Plasmonic Nanoparticles. *ACS Nano* **2010**, *4*, 2109–2123.
- (3) Lukianova-Hleb, E. Y.; Volkov, A. N.; Lapotko, D. O. Laser Pulse Duration Is Critical For the Generation of Plasmonic Nanobubbles. *Langmuir* **2014**, *30*, 7425–7434.
- (4) Lombard, J.; Biben, T.; Merabia, S. Kinetics of Nanobubble Generation Around Overheated Nanoparticles. *Phys. Rev. Lett.* **2014**, *112*, 105701.
- (5) Katayama, T.; Setoura, K.; Werner, D.; Miyasaka, H.; Hashimoto, S. Picosecond-to-Nanosecond Dynamics of Plasmonic Nanobubbles from Pump–Probe Spectral Measurements of Aqueous Colloidal Gold Nanoparticles. *Langmuir* **2014**, *30*, 9504–9513.
- (6) Hou, L.; Yorulmaz, M.; Verhart, N. R.; Orrit, M. Explosive Formation and Dynamics of Vapor Nanobubbles Around a Continuously Heated Gold Nanosphere. *New J. Phys.* **2015**, *17*, No. 013050.
- (7) Lombard, J.; Biben, T.; Merabia, S. Ballistic Heat Transport in Laser Generated Nanobubbles. *Nanoscale* **2016**, *8*, 14870–14876.
- (8) Nakajima, T.; Wang, X.; Chatterjee, S.; Sakka, T. Observation of Number-Density-Dependent Growth of Plasmonic Nanobubbles. *Sci. Rep.* **2016**, *6*, 28667.
- (9) Maheshwari, S.; van der Hoef, M.; Prosperetti, A.; Lohse, D. Dynamics of Formation of a Vapor Nanobubble Around a Heated Nanoparticle. *J. Phys. Chem. C* **2018**, *122*, 20571–20580.
- (10) Richardson, H. H.; Carlson, M. T.; Tandler, P. J.; Hernandez, P.; Govorov, A. O. Experimental and Theoretical Studies of Light-to-Heat Conversion and Collective Heating Effects in Metal Nanoparticle Solutions. *Nano Lett.* **2009**, *9*, 1139–1146.
- (11) Liu, Z.; Hung, W. H.; Aykol, M.; Valley, D.; Cronin, S. B. Optical Manipulation of Plasmonic Nanoparticles, Bubble Formation and Patterning of SERS Aggregates. *Nanotechnology* **2010**, *21*, 105304.
- (12) Baffou, G.; Polleux, J.; Rigneault, H.; Monneret, S. Super-Heating and Micro-Bubble Generation around Plasmonic Nanoparticles under cw Illumination. *J. Phys. Chem. C* **2014**, *118*, 4890–4898.
- (13) Baral, S.; Green, A. J.; Livshits, M. Y.; Govorov, A. O.; Richardson, H. H. Comparison of Vapor Formation of Water at the Solid/Water Interface to Colloidal Solutions Using Optically Excited Gold Nanostructures. *ACS Nano* **2014**, *8*, 1439–1448.
- (14) Liu, X.; Bao, L.; Dipalo, M.; De Angelis, F.; Zhang, X. Formation and Dissolution of Microbubbles on Highly-Ordered Plasmonic Nanopillar Arrays. *Sci. Rep.* **2016**, *5*, 18515.
- (15) Chen, J.; Saklayen, N.; Courvoisier, S.; Shen, Z.; Lu, J.; Ni, X.; Mazur, E. Dynamics of Transient Microbubbles Generated by fs-Laser

Irradiation of Plasmonic Micropylramids. *Appl. Phys. Lett.* **2017**, *110*, 153102.

(16) Zaytsev, M. E.; Lajoinie, G.; Wang, Y.; Lohse, D.; Zandvliet, H. J. W.; Zhang, X. Plasmonic Bubbles in n-Alkanes. *J. Phys. Chem. C* **2018**, *122*, 28375–28381.

(17) Lapotko, D. Plasmonic Nanoparticle-Generated Photothermal Bubbles and Their Biomedical Applications. *Nanomedicine* **2009**, *4*, 813–845.

(18) Emelianov, S. Y.; Li, P.-C.; O'Donnell, M. Photoacoustics for Molecular Imaging and Therapy. *Phys. Today* **2009**, *62*, 34–39.

(19) Baffou, G.; Quidant, R. Thermo-Plasmonics: Using Metallic Nanostructures as NanoSources of Heat. *Laser Photonics Rev.* **2013**, *7*, 171–187.

(20) Shao, J.; Xuan, M.; Dai, L.; Si, T.; Li, J.; He, Q. Near-Infrared-Activated Nanocalorifiers in Microcapsules: Vapor Bubble Generation for In Vivo Enhanced Cancer Therapy. *Angew. Chem., Int. Ed.* **2015**, *54*, 12782–12787.

(21) Liu, H.-L.; Fan, C.-H.; Ting, C.-Y.; Yeh, C.-K. Combining Microbubbles and Ultrasound for Drug Delivery to Brain Tumors: Current Progress and Overview. *Theranostics* **2014**, *4*, 432–444.

(22) Fan, Q.; Hu, W.; Ohta, A. T. Laser-Induced Microbubble Poration of Localized Single Cells. *Lab Chip* **2014**, *14*, 1572–1578.

(23) Krishnan, M.; Park, J.; Erickson, D. Optothermoeological Flow Manipulation. *Opt. Lett.* **2009**, *34*, 1976–1978.

(24) Zhang, K.; Jian, A.; Zhang, X.; Wang, Y.; Li, Z.; Tam, H.-y. Laser-Induced Thermal Bubbles for Microfluidic Applications. *Lab Chip* **2011**, *11*, 1389–1395.

(25) Zhao, C.; Xie, Y.; Mao, Z.; Zhao, Y.; Rufo, J.; Yang, S.; Guo, F.; Mai, J. D.; Huang, T. J. Theory and Experiment on Particle Trapping and Manipulation via Optothermally Generated Bubbles. *Lab Chip* **2014**, *14*, 384–391.

(26) Tantussi, F.; Messina, G. C.; Capozza, R.; Dipalo, M.; Lovato, L.; De Angelis, F. Long-Range Capture and Delivery of Water-Dispersed Nano-objects by Microbubbles Generated on 3D Plasmonic Surfaces. *ACS Nano* **2018**, *12*, 4116–4122.

(27) Xie, Y.; Zhao, C. An Optothermally Generated Surface Bubble and its Applications. *Nanoscale* **2017**, *9*, 6622–6631.

(28) Baffou, G.; Quidant, R. Nanoplasmonics for Chemistry. *Chem. Soc. Rev.* **2014**, *43*, 3898–3907.

(29) Adleman, J. R.; Boyd, D. A.; Goodwin, D. G.; Psaltis, D. Heterogeneous Catalysis Mediated by Plasmon Heating. *Nano Lett.* **2009**, *9*, 4417–4423.

(30) Wang, Y.; Zaytsev, M. E.; The, H. L.; Eijkel, J. C. T.; Zandvliet, H. J. W.; Zhang, X.; Lohse, D. Vapor and Gas-Bubble Growth Dynamics around Laser-Irradiated, Water-Immersed Plasmonic Nanoparticles. *ACS Nano* **2017**, *11*, 2045–2051.

(31) Wang, Y.; Zaytsev, M. E.; Lajoinie, G.; The, H. L.; Eijkel, J. C. T.; van den Berg, A.; Versluis, M.; Weckhuysen, B. M.; Zhang, X.; Zandvliet, H. J. W.; et al. Giant and Explosive Plasmonic Bubbles by Delayed Nucleation. *Proc. Natl. Acad. Sci. U. S. A.* **2018**, *115*, 7676–7681.

(32) Florschuetz, L. W.; Chao, B. T. On the Mechanics of Vapor Bubble Collapse. *J. Heat Transfer* **1965**, *87*, 209.

(33) Plesset, M. S.; Prosperetti, A. Bubble Dynamics and Cavitation. *Annu. Rev. Fluid Mech.* **1977**, *9*, 145–185.

(34) Brennen, C. E. *Cavitation and Bubble Dynamics*; Oxford University Press: Oxford, 1995.

(35) Legendre, D.; Borée, J.; Magnaudet, J. Thermal and Dynamic Evolution of a Spherical Bubble Moving Steadily in a Superheated or subcooled Liquid. *Phys. Fluids* **1998**, *10*, 1256–1272.

(36) Hao, Y.; Prosperetti, A. The Dynamics of Vapor Bubbles in Acoustic Pressure Fields. *Phys. Fluids* **1999**, *11*, 2008–2019.

(37) Hao, Y.; Prosperetti, A. The Collapse of Vapor Bubbles in a Spatially non-Uniform Flow. *Int. J. Heat Mass Transfer* **2000**, *43*, 3539–3550.

(38) Prosperetti, A. Vapor Bubbles. *Annu. Rev. Fluid Mech.* **2017**, *49*, 221–248.

(39) Pavlov, P. A. Fast Collapse of a Vapor Bubble. *Int. J. Heat Mass Transfer* **2017**, *104*, 627–633.

(40) Nigmatulin, R. I.; Khabeev, N. S. Dynamics of Vapor-Gas Bubbles. *Fluid Dyn.* **1976**, *11*, 867–871.

(41) Nigmatulin, R. I.; Khabeev, N. S.; Nagiev, F. B. Dynamics, Heat and Mass Transfer of Vapour-Gas Bubbles in a Liquid. *Int. J. Heat Mass Transfer* **1981**, *24*, 1033–1044.

(42) Hao, Y.; Zhang, Y.; Prosperetti, A. Mechanics of Gas-Vapor Bubbles. *Phys. Rev. Fluids* **2017**, *2*, No. 034303.

(43) Le-The, H.; Berenschot, E.; Tiggelaar, R. M.; Tas, N. R.; van den Berg, A.; Eijkel, J. C. T. Shrinkage Control of Photoresist for Large-Area Fabrication of Sub-30 nm Periodic Nanocolumns. *Adv. Mater. Technol.* **2017**, *2*, 1600238.

(44) Baffou, G.; Berto, P.; Bermúdez Ureña, E.; Quidant, R.; Monneret, S.; Polleux, J.; Rigneault, H. Photoinduced Heating of Nanoparticle Arrays. *ACS Nano* **2013**, *7*, 6478–6488.

(45) Epstein, P. S.; Plesset, M. S. On the Stability of Gas Bubbles in Liquid-Gas Solutions. *J. Chem. Phys.* **1950**, *18*, 1505–1509.

■ NOTE ADDED AFTER ASAP PUBLICATION

This paper was published ASAP on February 27, 2020. Equation 2 was updated. The revised paper was reposted on March 2, 2020.